npj | biosensing

Article

https://doi.org/10.1038/s44328-026-00083-0

An integrated electrochemical platform for low-volume biosensing

Check for updates

Fatma Kurul[1,2], Damla Aydogan[1,3], Dogukan Topcu[1], Furkan Kocer[1,3], Ünal Akar[4,5,6], Ali Koşar[4,5,6], Arif E. Cetin[1,7] ✉ & Seda Nur Topkaya[1,8] ✉

We present a fully integrated, low-cost electrochemical sensing platform that combines a custom 3D-printed flow cell, a microfluidic pumping module, and a C# GUI for synchronized control, acquisition, and on-board analysis. The system addresses limitations of conventional SPE workflows by automating delivery–measure–rinse sequences and stabilizing flow, enabling reproducible measurements with an effective contact volume of ~15 µL (per-run sample load ~45 µL including upstream volume). Using dsDNA as a model analyte, chronoamperometry under continuous flow yielded a linear calibration across 100–1000 µg/mL ($R^2 \approx 0.965$). Limited SPE reuse was supported by an electrochemical regeneration step, e.g., the first cycle preserved ~90% of the initial signal with similar peak structure, a second cycle produced reduced but qualitatively usable responses, while further cycles showed substantial attenuation/broadening. Under matched conditions, the platform achieved comparable signal to pipette-based delivery with improved reproducibility, reduced baseline drift, and shorter hands-on time. The GUI integrates instrument control with automated dilution calculators and real-time visualization, minimizing operator variability. These results establish a compact, programmable chassis for low-volume SPE assays with straightforward adaptation to point-of-care and field contexts.

Electrochemical sensor systems have emerged as analytical tools in modern chemistry, offering real-time, sensitive, and selective detection of chemical and biological analytes through the analysis of redox reactions at electrode interfaces[1]. Their advantages, including high sensitivity, rapid response, cost-effectiveness, low power consumption, ease of miniaturization, and compatibility with small sample volumes, have made them particularly attractive for a broad range of applications, including clinical diagnostics, environmental monitoring, food safety, and industrial process control[2–7]. A conventional electrochemical system typically consists of a chamber housing an electrode assembly immersed in an electrolyte solution, and a potentiostat that applies controlled potentials and records current responses. The electrode assembly generally comprises a working electrode (WE), a counter electrode (CE), and a reference electrode (RE)[8]. The WE is the site of the electrochemical reaction, the CE completes the circuit, and the RE provides a stable potential reference, ensuring accurate and reproducible measurements[9]. This three-electrode configuration enables precise control over electrochemical processes, which is critical for obtaining reliable analytical results[10]. In electrochemical biosensing, signals arise either from Faradaic charge transfer (redox of target or reporter species) or from non-Faradaic/capacitive changes at the interface; voltammetric and amperometric techniques transduce these processes into quantitative readouts[11]. Differential pulse voltammetry (DPV) enhances peak resolution and sensitivity for surface-bound redox events[12], cyclic voltammetry (CV) maps redox behavior and surface activation[13], and chronoamperometry (CA) tracks current at a fixed potential to follow adsorption/reaction kinetics in real time[14]. On carbon SPEs, nucleobase oxidation (e.g., guanine, adenine) provides a convenient label-free model for method validation.

Recent advances in screen-printing techniques have led to the widespread adoption of screen-printed electrodes (SPEs), which integrate the three-electrode system into a compact, planar format[15]. These disposable electrodes can be fabricated using conductive inks, e.g., carbon, silver, gold, or platinum, printed on substrates such as ceramic, plastic, or paper[16,17].

[1]Izmir Biomedicine and Genome Center, Balcova, Izmir, Turkey. [2]The Graduate School of Natural and Applied Sciences, Department of Nanoscience and Nanoengineering, Dokuz Eylul University, Buca, Izmir, Turkey. [3]Department of Biomedical Engineering, Faculty of Engineering and Architecture, Izmir Bakircay University, Menemen, Izmir, Turkey. [4]Faculty of Engineering and Natural Sciences, Sabanci University, Tuzla, Istanbul, Turkey. [5]Sabanci University Nanotechnology and Application Center (SUNUM), Sabanci University, Tuzla, Istanbul, Turkey. [6]Center of Excellence for Functional Surfaces and Interfaces for Nano-Diagnostics (EFSUN), Sabanci University, Tuzla, Istanbul, Turkey. [7]Department of Biophysics, Faculty of Medicine, Dokuz Eylul University, Balcova, Izmir, Turkey. [8]Izmir International Biomedicine and Genome Institute, Dokuz Eylul University, Balcova, Izmir, Turkey. ✉e-mail: arifengin.cetin@ibg.edu.tr; sedanur6@gmail.com

Owing to their reproducibility and suitability for portable sensing platforms, SPEs have become essential components in point-of-care diagnostic devices[18,19]. Their planar design facilitates analysis of microliter-scale biological samples of biological fluids[20,21], e.g., including blood[22], saliva[23], sweat[24], and urine[25], making them highly relevant for decentralized healthcare applications. However, despite their advantages, SPEs suffer from certain limitations, including uneven sample distribution and operator-dependent variability[26]. During pipette-based loading, the sample droplet often forms a curved meniscus that varies from one experiment to another, resulting in inconsistent electrode coverage and reduced measurement accuracy and reproducibility. Moreover, the single-use nature of SPEs increases operational costs, particularly in high-throughput or resource-limited settings.

Microfluidic control is central to overcoming these limitations as delivery in small channels is predictably laminar, enabling well-defined residence times and diffusion-limited mixing[27,28]. In the low-Reynolds-number regime typical of microchannels, convective–diffusive transport can be engineered via flow setpoints, channel geometry, and surface chemistry (often summarized by the Péclet number), yielding repeatable exposure of analyte to the electrode and suppressing evaporation/handler effects[29]. In this regime, analyte delivery to the electrode can be engineered through setpoint flow rates, channel geometry, and surface chemistry, e.g., reducing operator variability and evaporation artifacts. Over the past two decades, microfluidics for chemical sensing has evolved from glass/silicon chips to soft lithography in polydimethylsiloxane (PDMS), paper-based capillary devices[30], digital microfluidics[31], centrifugal lab-on-disc[32], and, more recently, rapid additive manufacturing, e.g., 3D printing[33]. In parallel, fluid actuation progressed from external pressure sources and syringe pumps to compact on-board solutions, e.g., miniature piezoelectric pumps, integrated valve manifolds, and closed-loop flow with inline sensing, enabling scripted delivery-measure-rinse cycles and sample-to-answer operation. These evolutionary steps, such as material diversification, on-board actuation, and feedback control, have made it feasible to pair SPEs with reproducible, low-volume flow environments suitable for quantitative assays.

To address these challenges and enhance the performance of SPE-based sensing systems, additive manufacturing, particularly 3D-printing, has been increasingly integrated into sensor platform development. 3D-printing enables the rapid, cost-effective, and customizable fabrication of components such as flow cells, microfluidic interfaces, and sensor housings, tailored to specific analytical tasks[34]. These custom structures improve sample handling, enhance reproducibility, and facilitate miniaturization, which are critical requirements in current electrochemical diagnostics. To address this need, both commercial and academic efforts have focused on developing flow cells specifically designed for seamless integration with SPEs. For instance, commercial solutions such as Metrohm AG Flow Cell for SPEs (CFLWCL-WE) and Zensor R&D Co.'s Electrochemical Flow Cell (SF100) offer inlet-outlet-controlled flow architectures but lack built-in automation or active pumping mechanisms. According to the literature, various 3D-printed flow cell configurations have been proposed to enhance the utility of SPEs. Siller et al. developed static and dynamic 3D-printed flow cells that improved aptamer-based impedimetric detection of *Escherichia coli*, incorporating micromixing and selective electrode exposure at a cost ($18) significantly lower than commercial options[34]. Similarly, Contreras-Naranjo et al. introduced a modular 3D-printed fluidic electrochemical sensing platform with a screw-based seal, demonstrating enhanced dopamine detection sensitivity and robust reusability, e.g., $9.81 fabrication cost[35]. Further innovations include a polydimethylsiloxane (PDMS)-based microfluidic chip developed by Chen et al. for prostate-specific antigen detection, offering a rapid, cost-effective alternative to traditional fabrication[36], and a miniature fluidic system fabricated using multilayer ceramic technology and low-temperature co-fired ceramics by Kuscer et al., which improved flow reproducibility and robustness over traditional or printed devices[37]. Additionally, Ruiz-Vega et al. reported a paper-based microfluidic SPE platform for magneto-immunosensing of matrix metalloproteinase 9, achieving ELISA-comparable sensitivity (LOD: 0.01 ng/mL) with reduced assay time (~10 min)[38]. Recent work on automated microfluidic electrochemical sensors has expanded demonstration platforms at the intersection of fluidic handling and sensing performance, including approaches that embed microfluidics for enhanced detection in point-of-care formats. For example, emerging microfluidic biosensor architectures that leverage integrated actuation and control demonstrate improved analytical reproducibility and sample handling characteristics[39,40].

Although these developments represent significant progress toward cost-effective and reproducible SPE-based electrochemical diagnostics, none of the reported flow cells includes an integrated pumping mechanism, relying instead on external pumps or manual injections for sample delivery. This limitation reduces automation potential and can hinder deployment in resource-limited or fully autonomous point-of-care applications. Therefore, there remains a clear need for low-cost, reusable, and fully integrated flow cell systems that not only host SPEs but also automate fluid handling for enhanced reproducibility and usability[41,42].

We recently introduced an incubator-integrated electrochemical platform for cell-based analyses, which serves as a methodological precursor to the present benchtop, low-volume molecular SPE system[43]. By comparison, the present study targets benchtop, low-volume molecular biosensing on SPEs and therefore operates under a different objective and regime. While that prior system, enabling cell adhesion/proliferation and drug-response measurements at 37 °C and 5% CO_2, shared enabling blocks, e.g., 3D-printed flow cell, PID-regulated (Proportional-Integral-Derivative) microfluidics, and a C#-based GUI, its focus was cell-based analysis inside or coupled to an incubator. Here, we emphasize a serial-injection workflow, e.g., ~15 µL per run, a head-to-head comparison of flow versus pipetted delivery, and quantified SPE reuse limits via electrochemical regeneration. These goals required distinct flow-cell geometry, assay sequencing, data-analysis modules, and evaluation metrics tailored to molecular detection rather than cell studies. Consistent with these aims, the present work opts for CA as the primary readout under closed-loop flow (fixed-potential monitoring compatible with short residence times), complemented by DPV for peak-resolved characterization and CV for diagnostic checks and surface activation, e.g., this suite of methods provides label-free detection on carbon SPEs while aligning with low-volume, programmable operation.

To address the above gap, we present an integrated platform that unifies closed-loop fluid control, single-cycle electrode regeneration, and operator-friendly software in a single architecture. We developed a fully integrated, low-cost electrochemical sensing platform that incorporates a custom-designed 3D-printed flow cell, an embedded pumping and valve manifold, a regeneration module that restores the SPE surface through controlled potential application for limited repeated use, and a user-friendly graphical user interface (GUI) (Fig. 1A, B). Prior to measurements, the SPE is electrochemically activated to increase the density of electroactive sites and improve interfacial charge transfer, supporting reproducible adsorption-controlled responses. To validate the system characteristics, we employed dsDNA as a model analyte. In contrast to previously reported systems, our platform executes programmable delivery-measure-rinse sequences under closed-loop control, significantly reducing operator variability and enabling targeted analyte delivery to the sensing zone. The flow cell supports precise control over small-scale sample volumes, e.g., 15 µL, facilitates uniform exposure of the electrode surface, and eliminates reliance on external pumps by incorporating on-board actuation. Moreover, the platform features a C#-based GUI that not only controls hardware components, e.g., embedded pumps, valves, and the potentiostat, but also automates measurement protocols, data acquisition, and real-time signal processing. The GUI includes dedicated modules for biosensing signal generation via electrochemical techniques, e.g., differential pulse voltammetry (DPV), cyclic voltammetry (CV), and chronoamperometry (CA). It further supports peak analysis and quantitative calibration curve generation, as well as limit of detection and limit of quantitation (LOD/LOQ) calculation, ensuring a robust and streamlined workflow for end-users. Importantly, regeneration is framed as limited reuse: the first regeneration

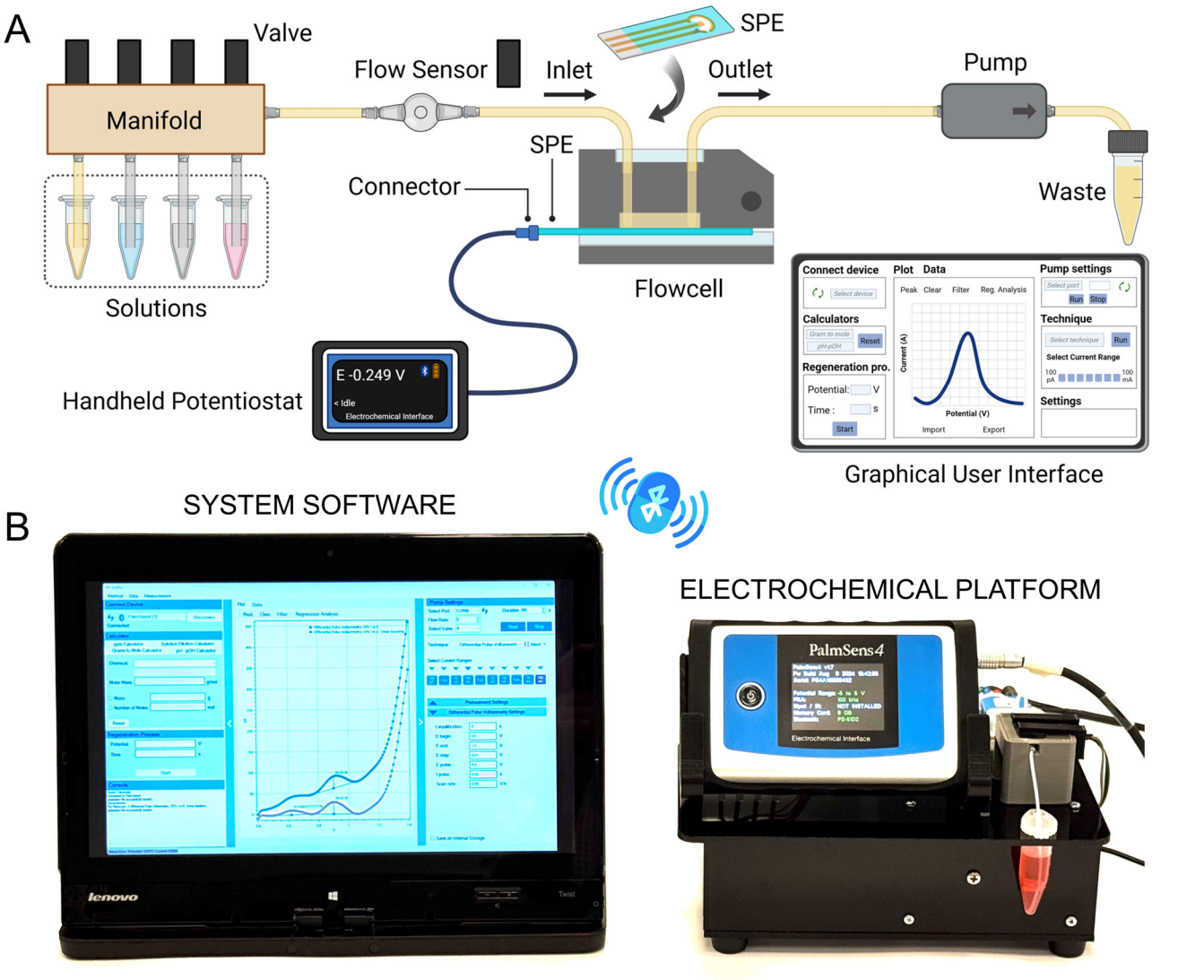


Fig. 1 | Integrated electrochemical platform architecture and system overview. **A** Schematic illustration of the system architecture, comprising the flow cell, the microfluidic pumping module, the potentiostat, and the system software. Created with BioRender.com. **B** Photograph of the platform, showing the system software with a custom-designed GUI for electrochemical measurements and the electrochemical platform consisting of a compact handheld potentiostat and the flow cell, enabling portable and user-friendly biosensing operations.

preserves comparable behavior (~90% of the initial signal), whereas additional cycles show progressive attenuation and peak broadening. This limited reusability can modestly reduce consumable use and, for the first regeneration, maintain comparable measurement behavior.

Unlike prior SPE flow cells that depend on external pumps or manual delivery, the present system integrates closed-loop, programmable serial injections (~15 µL) with head-to-head delivery benchmarking and a defined single-cycle reuse window-capability not jointly addressed in existing devices. In addition, the platform includes automated sample preparation utilities, allowing users to input reagent volumes and concentrations, which are used to calculate required dilutions and operational parameters prior to analysis. Collectively, this platform represents a comprehensive electrochemical sensing solution that bridges the gap between low-cost fabrication and high analytical accuracy. By consolidating fluidic control, sensing, data analysis, and electrode regeneration into a single automated system, it significantly advances the capabilities of SPE-based platforms for point-of-care diagnostics, environmental analysis, and resource-limited settings, where portability, precision, and autonomy are paramount.

The primary novelty of this study lies in the system-level integration of fluid handling, measurement execution, and analysis into a single, programmable chassis for SPE assays, rather than in optimizing a single target chemistry. Specifically, the platform combines a precision-sealed, low-volume 3D-printed flow cell with on-board actuation and PID-regulated closed-loop flow, scripted delivery-measure-rinse routines, limited electrochemical regeneration, and a custom GUI enabling synchronized acquisition and on-board analysis. This level of synchronization and automation is not achievable with conventional manual or pipette-based SPE workflows or modular flow setups. This integration delivers quantitative workflow advantages over conventional pipette-based SPE operation and modular flow setups, including a defined effective contact volume of ~15 µL, improved reproducibility (CV~3% under closed-loop flow vs. ~8% for pipetted delivery under matched conditions), reduced carryover (< 1%), lower baseline drift, and shorter hands-on time (~10–15 s. per run). While alternative ultra-low-volume or chemistry-specialized microfluidic systems can achieve lower absolute volumes or sensitivities through assay-specific amplification, such approaches often trade accessibility, cost, or assay generality for these extremes. In contrast, the present work emphasizes reproducibility and broad usability using off-the-shelf SPEs and low-cost components (~$6 flow cell), providing a generalizable platform that can be readily paired with application-specific surface chemistries in follow-on studies.

Results

Flow cell

The custom-designed electrochemical flow cell, with overall dimensions of 25 × 33 × 20 mm, consists of a modular assembly comprising a top cover, a bottom cover, a PDMS support layer functioning as an SPE holder, and an elastomeric O-ring, as illustrated in Fig. 2A. The top cover features a groove with 1.5 mm depth and dimensions of 8 mm inner diameter and 11 mm outer diameter to accommodate the O-ring, thereby ensuring reliable sealing. The housing structure was fabricated using SLA-based 3D printing (Formlabs Form3), offering high geometric precision (layer resolution is between 25 and 100 μm) and strong mechanical properties due to the use of clear resin material, while also enabling in situ visualization of fluid dynamics. The top cover includes two aligned fluidic ports, e.g., inlet and outlet, for pump-driven flow control, while the bottom cover accommodates the SPE in a rectangular cavity, lined with a 3 mm PDMS layer to act as a soft mechanical cushion, protecting the electrode surface during assembly. In Fig. 2B, the yellow-highlighted circular region represents the sample well, which is designed to align with and cover the full three-electrode configuration of the SPE, ensuring uniform fluid delivery across the active sensing area. This well defines an internal chamber volume of approximately 15 μL, which corresponds to the effective volume in contact with the SPE during measurements. For each measurement, a~45 μL sample plug is loaded and dispensed at

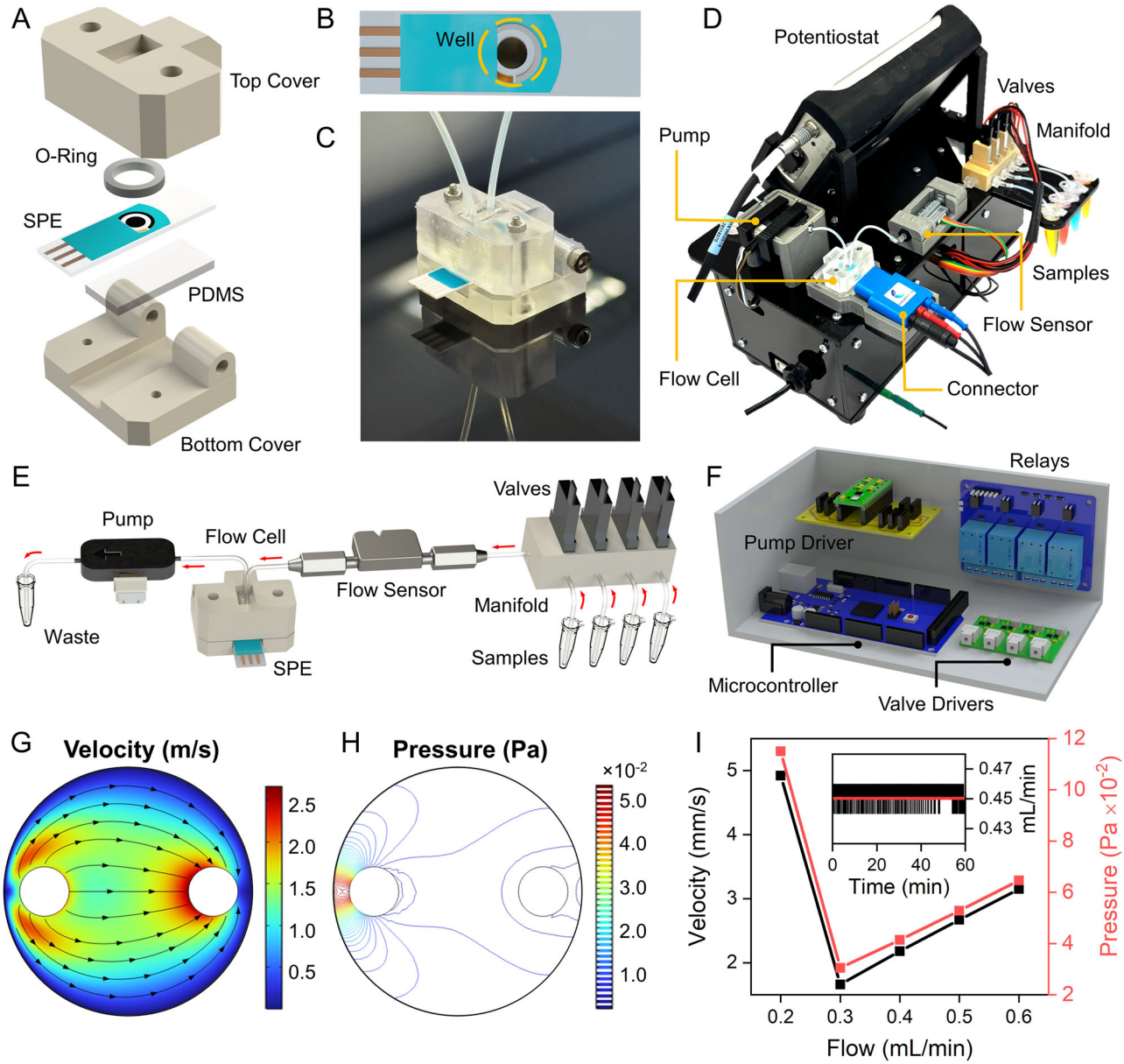


Fig. 2 | Flow cell architecture, microfluidic integration, and flow characterization. A Exploded view of the modular flow cell assembly, comprising the top cover with fluidic ports, an elastic O-ring for sealing, SPE, a PDMS support layer, and the bottom cover. **B** Top-view schematic of the SPE showing the sample well (highlighted in dashed yellow) aligned with the working electrode. **C** Photograph of the flow cell with SPE inserted and fluidic tubing connected. **D** Overview of the complete integrated system featuring the microfluidic pumping module and potentiostat mounted in a portable enclosure. **E** Schematic diagram of the fluidic routing: liquid samples from tubes are selectively directed through solenoid valves and a manifold, pass through a flow sensor, reach the flow cell where the SPE is located, and exit to waste via a piezoelectric pump. **F** Internal electronics enclosure housing the pump driver, valve drivers, relays, and a central microcontroller for automated fluidic control and signal processing. **G** CFD simulation showing the velocity field distribution. **H** Corresponding pressure map derived from CFD analysis, confirming low-pressure drops and uniform distribution. **I** Experimentally measured velocity (black) and pressure (red) values as a function of flow rate. The inset demonstrates the temporal flow rate stability maintained using a PID-based feedback controller over a 60-minoperation period. The slight feature between 0.2 and 0.3 mL/min lies within the pressure-sensor noise floor and reflects PID micro-adjustments rather than true non-monotonic hydraulics; repeated runs ($n = 3$) confirmed an underlying monotonic trend.

Table 1 | Side-by-side benchmark of delivery modes under matched conditions (dsDNA 500 µg/mL, *n* = 5)

Metric	Pipette drop (Static)	Flow cell (closed-loop)
Mean current (µA)	36.8	35.9
Reproducibility (CV, %)	8.2	3.1
Effective contact volume (µL)	~15	~15
Total sample per run (µL)	~20	~45
Hands-on time (s)	45–60	10–15
Total time to result (s)	120–150	90–120
Baseline drift (µA/min)	0.9	0.2
Carryover after blank (%)	4.5	0.8
Operator-to-operator CV (%)	10.4	3.6

0.5 mL/min. This plug comprises ~15 µL occupying the chamber immediately above the SPE and ~30 µL residing in the upstream tubing (ID: 0.8 mm and length: 6 cm). During acquisition, only the ~15 µL chamber volume contacts the electrode, e.g., the remaining volume maintains steady, laminar flow. Unless otherwise noted, "sample loaded per run" refers to ~45 µL, whereas "effective contact volume" refers to ~15 µL. To ensure leak-free operation, the design incorporates a custom O-ring made of elastic resin, seated in a grooved channel surrounding the sample well with dimensions of 8 mm inner diameter, 11 mm outer diameter, and 1.75 mm depth. This O-ring conforms to small imperfections or roughness on the surface, providing mechanical stability and forming a robust sealing mechanism upon tightening the assembly with stainless-steel screws and nuts at either end. The full assembly is shown in Fig. 2C, where the inlet and outlet tubes are visibly fixed into place, ensuring secure, pressure-resistant operation.

The flow cell design provides reliable leak-free operation through a precision O-ring and robust fastening, ensuring stability under continuous flow and back-pressure. It also enables secure electrical interfacing of the SPE, maintaining signal stability during measurements. The modular design ensures reusability, compatibility with different SPE formats, and easy integration into portable or automated platforms. Its controlled flow over the electrode enhances reproducibility, reduces dead volume, improves analyte delivery, and provides uniform sensing area coverage for reliable electrochemical signals (Table 1).

Microfluidic pumping module

To enable high-precision, automated electrochemical analysis, the custom-designed flow cell was integrated into a compact and fully programmable microfluidic pumping module. As shown in Fig. 2D, the microfluidic pumping module is positioned behind the potentiostat within the assembled system. The module features a tightly coordinated configuration consisting of a piezoelectric micropump (Bartels Mikrotechnik GmbH), a 4-channel manifold, four solenoid valves (Takasago Electric, Inc.), and a high-sensitivity flow sensor (Sensirion AG), as illustrated in Fig. 2E. The pump provides consistent and pulsation-free fluid delivery, while the valve array enables automated selection of up to four distinct fluid sources. Notably, the pump is located at the downstream end of the fluidic circuit and operates in suction mode, pulling liquid samples from the sample tubes through the manifold, valves, and flow sensor, then directing them to the flow cell and ultimately to the waste outlet. This configuration minimizes pressure spikes and avoids dead volumes, ensuring smooth flow and enhanced reproducibility. Each valve is individually actuated via relay-controlled drivers, enabling precise digital fluid routing. The flow sensor is strategically positioned immediately upstream of the flow cell, where it provides real-time volumetric flow data with high sensitivity. These data are transmitted to a central microcontroller, which implements a closed-loop control scheme based on a PID (Proportional-Integral-Derivative) algorithm to maintain flow rate stability (See Supplementary Information for the details of the PID algorithm). This real-time feedback mechanism ensures tight regulation of fluid delivery, especially critical in low-volume electrochemical assays. As illustrated in the inset of Fig. 2I, the PID-regulated flow control system achieves highly stable flow delivery, with minimal fluctuations around the target rate (e.g., 0.45 mL/min). The narrow amplitude of variation confirms the effectiveness of the implemented control strategy in maintaining flow uniformity, which is especially critical for low-volume, time-sensitive electrochemical assays. This level of stability ensures reproducible interaction between the analyte and electrode surface, thereby improving the overall reliability and precision of sensing measurements.

The number of fluid lines was set to four, assigned to sample, conditioning/binding buffer, rinse, and regeneration/blank (or waste bypass), enabling a complete delivery–measure–rinse–regenerate sequence without reconfiguration. This design balances throughput, carryover control (dedicated rinse and regeneration lines), and system complexity. The control firmware and GUI are modular; if future applications demand more lines, the architecture can be extended via additional inlets (e.g., valve multiplexing or an added manifold).

The pump driver module is digitally operated via an I2C communication protocol, allowing dynamic adjustment of both frequency and output voltage parameters through software. A four-channel relay unit controls the valve actuation, supporting multi-sample protocols and enabling flexible flow path configurations. All hardware components including the pump, valves, sensor, and flow cell, are synchronized under the control of the microcontroller, ensuring stable and reliable operation throughout the analysis cycle (See Supplementary Information regarding the firmware running on the microcontroller for hardware control). As shown in Fig. 2F, the electronic enclosure includes the driver circuits, relay modules, and the microcontroller unit, all housed in a compact enclosure beneath the fluidic platform. The plug-and-play modularity of the system facilitates easy replacement or reconfiguration of components, enabling user-friendly customization for various sensing protocols. The valve block is positioned immediately upstream of the flow cell and connected with short 1/4-28 leads to 0.8 mm-ID tubing to minimize wetted volume. After each switch, the GUI scripts a forward-flush of two-three chamber volumes (~30–45 µL for a 15 µL chamber) using rinse, followed by optional regeneration/blank to further reduce residuals. Purge volumes are specified in multiples of chamber volume to facilitate replication across builds. This integrated architecture removes manual pipetting, improves reproducibility, minimizes contamination and reagent use, and provides a scalable platform for point-of-care, environmental, and multiplexed biosensing with minimal user input.

Computational fluid dynamics (CFD) simulations

CFD simulations were performed using COMSOL Multiphysics® 6.1 based on the Finite Element Method (FEM) to characterize the steady-state laminar flow behavior within the electrochemical flow cell, particularly focusing on velocity profiles and species delivery relevant to sensor performance. The working fluid was defined as incompressible and Newtonian, with a density of 1000 kg/m^3 and a dynamic viscosity of 0.99 cP (0.00099 Pa·s). The fluid was assumed to be Newtonian and incompressible, and the flow was presumed to be steady state throughout the simulations. The flow field was obtained by solving the incompressible Navier-Stokes and continuity equations:

$$\rho(\boldsymbol{u}\cdot\nabla\boldsymbol{u}) = -\nabla\rho + \mu\nabla^2\boldsymbol{u} \tag{1}$$

$$\nabla.\boldsymbol{u} = \boldsymbol{0} \tag{2}$$

where ρ is the density, $\boldsymbol{u}$ is the velocity field, and μ is the dynamic viscosity. A convection–diffusion equation was additionally solved:

$$\frac{\partial c}{\partial t} = D\nabla^2 c - \boldsymbol{u}\cdot\nabla c \tag{3}$$

where c is the species concentration, and D is the diffusion coefficient. The no-slip boundary condition was implemented at all internal channel walls,

and the outlet boundary condition was established at zero-gauge pressure. To verify laminar flow conditions, the Reynolds number was calculated for each inlet flow rate, e.g., $Re = \rho u D_h/\mu$, where u is the average fluid velocity and D_h is the hydraulic diameter, $D_h = 4A/P$. In this relation, A is the cross-sectional area and P is the wetted perimeter of the channel, i.e., D_h was computed as the diameter of the tubing, e.g., 1.8 mm.

As shown in Fig. 2I, we investigated five different inlet flow rates 0.2, 0.3, 0.4, 0.5, and 0.6 mL/min, corresponding to volumetric flow rates between 3.33×10^{-9} and 1.00×10^{-8} m^3/s. These were converted to average inlet velocities using the relation: $u = Q/A$, where Q is the flow rate and A is the cross-sectional area of the inlet channel. The computed Reynolds numbers fluctuated between 2.4 and 7.2 across all experimental conditions, confirming the laminar flow regime well below the transitional threshold ($Re \ll 2000$). The full momentum transport was governed by the Navier-Stokes form, including body forces, e.g., pressure gradients. Additionally, the transport of diluted species was modeled using the convection-diffusion equation to represent potential electrochemical species during deposition and stripping processes. All simulations were conducted under steady-state assumptions $(\partial/\partial t = 0)$, and gravitational or external forces were neglected.

The simulation outputs depicted in Fig. 2G–I offer critical insights into the fluid dynamics within the custom-designed flow cell. Figure 2G presents the velocity magnitude distribution across the circular sensing chamber at a representative flow rate. As typical for laminar flow, the velocity profile shows a symmetric parabola, with peak velocities along the central streamline between inlet and outlet. Flow accelerates at the narrow inlet and spreads across the circular chamber for uniform analyte distribution, while reduced velocities near the walls reflect the no-slip boundary condition. An unstructured triangular mesh with local refinement around the inlet and outlet was generated. To ensure numerical convergence, four mesh densities (coarse, fine, extra fine, extremely fine) were evaluated. The steady-state maximum centerline velocity u_{max}, at an inlet flow rate of 0.5 mL/min was used as the mesh sensitivity metric. The domain and boundary element counts, together with u_{max}, are reported in Supplementary Table 1. The change in u_{max}, between the fine and extra fine meshes was only 0.37%, and the solution became identical between the extra fine and extremely fine meshes, e.g., 0% difference, demonstrating full mesh independence. Even the difference between the coarse and fine meshes remained below 2%. For this reason, selecting the fine mesh is the most scientifically reasonable choice, as it provides identical accuracy at significantly lower computational cost. The velocity field confirms efficient flushing of the sensing zone, with no stagnation or recirculation that could affect reproducibility. Figure 2H illustrates the corresponding pressure contours, indicating a smooth pressure gradient from inlet to outlet. The overall pressure drop remains minimal across the domain ($< 1.2 \times 10^{-2}$ Pa), verifying that the system operates in a low-pressure, energy-efficient regime compatible with portable pumping systems. Minor pressure changes near the inlet and outlet reflect local constrictions but do not disturb laminar flow, while the chamber's circular geometry distributes resistance symmetrically and minimizes shear stress variations on the electrode. These simulations are not intended to reveal new fluid-dynamic behavior, but rather to validate the engineering design of the flow cell by confirming laminar, uniform, and low-pressure transport conditions that are essential for reproducible analyte delivery, minimized dead volume, and stable electrochemical signals. Thus, CFD serves as a design and performance verification tool linking fluidic behavior directly to measurement reliability.

Figure 2I summarizes the quantitative relationship between volumetric flow rate (0.2–0.6 mL/min), average velocity (black curve, left y-axis), and pressure drop (red curve, right y-axis). An unexpected non-monotonic behavior is observed at 0.2 mL/min, where both pressure and velocity exhibit anomalously high values compared to other flow rates. This likely arises from entry effects at very low flow regimes, where insufficient fluid inertia leads to local backpressure and jetting phenomena. Beyond 0.3 mL/min, both parameters increase monotonically with flow rate, consistent with theoretical predictions for Newtonian laminar flow. These trends confirm that flow stability and controllability improve with moderate flow rates (0.3–0.6 mL/min), providing a robust operational window for electrochemical sensing applications. The custom flow cell supports stable laminar transport under low pressure, ensuring uniform analyte delivery without flow instabilities. Operating at 0.3–0.6 mL/min, it provides efficient reagent use, precise fluid control, and reproducible performance, making it well-suited for portable electrochemical sensing platforms. As an additional note, experimental flow–pressure data were acquired under PID-regulated operation while logging flow (GUI) and pressure (transducer output) simultaneously. At the lowest set points (0.2–0.3 mL/min), the device pressure drop approaches the sensor's resolution, producing small apparent fluctuations when the controller applies corrective micro-steps. To assess reproducibility, the sweep (0.2–0.6 mL/min) was repeated in three independent runs; all runs showed the same overall monotonic trend, and the minor feature near 0.3 mL/min was not consistently observed, indicating measurement noise rather than a physical departure from laminar behavior.

Electrochemical activation

Electrochemical impedance spectroscopy (EIS) was employed to investigate the impedance changes of the electrode surface before and after the electrochemical activation process[44]. For this purpose, two groups of SPEs were prepared, e.g., the first group ($n = 3$) underwent electrochemical activation, while the second group ($n = 3$) was left untreated. The activation procedure was performed in ACB (pH 4.8) by applying +1.8 V for 60 s. EIS measurements were conducted for both the activated and non-activated electrode groups using an electrochemically active redox probe consisting of 10 mM $K_4[Fe(CN)_6]/K_3[Fe(CN)_6]$ (702587, Sigma-Aldrich, Germany) in 0.1 M KCl (P9541, Sigma-Aldrich, Germany). As shown in Fig. 3A, a semicircle with a larger diameter is observed at the non-activated SPE (red curve) in the low-frequency range, while the diameter of the semicircle diminished at the activated SPE (black curve). This shows that the electrochemical pretreatment process considerably affects the surface impedance properties, leading to a more favorable charge-transfer behavior. In particular, the activation step significantly reduced the charge-transfer resistance (R_{ct}), demonstrating enhanced interfacial electron-transfer kinetics. The EIS spectra were analyzed by fitting the experimental data to a simplified Randles equivalent circuit using the ZView software (Fig. 3C—inset). The average R_{ct} value of the activated SPEs (~0.077 kΩ) was substantially lower than that of the non-activated SPEs (~0.21 kΩ), confirming that the electrochemical activation performed in ACB (pH 4.8) effectively improved their electrochemical performance. Overall, the R_{ct} value decreased by approximately threefold after activation, clearly indicating enhanced electron-transfer kinetics.

Electrochemical detection of dsDNA via flow-based chronoamperometry

Having established stable, low-volume delivery over the SPE, we next assessed quantitative readout under flow using dsDNA as a benchmark target biomolecule through chronoamperometry (Fig. 3B, C). In this engineering study, dsDNA serves as a model analyte to benchmark closed-loop, low-volume operation. The signal arises from adsorption of nucleic acids onto the activated carbon SPE followed by potential-resolved oxidation of nucleobases under controlled flow; thus, "label-free" denotes no external tags and electrochemical selectivity, not biorecognition by a capture probe. To evaluate the analytical performance of the developed platform, double-stranded DNA (dsDNA) from calf thymus was employed as a model analyte. The flow cell was employed to ensure the targeted delivery of dsDNA onto the SPE surface. To assess the capability of the integrated microfluidic system for electrochemical DNA detection, chronoamperometry was employed to detect dsDNA at different concentrations. This method was selected for these experiments as it enables real-time monitoring of current changes following the introduction of analyte molecules onto the electrode surface. Different

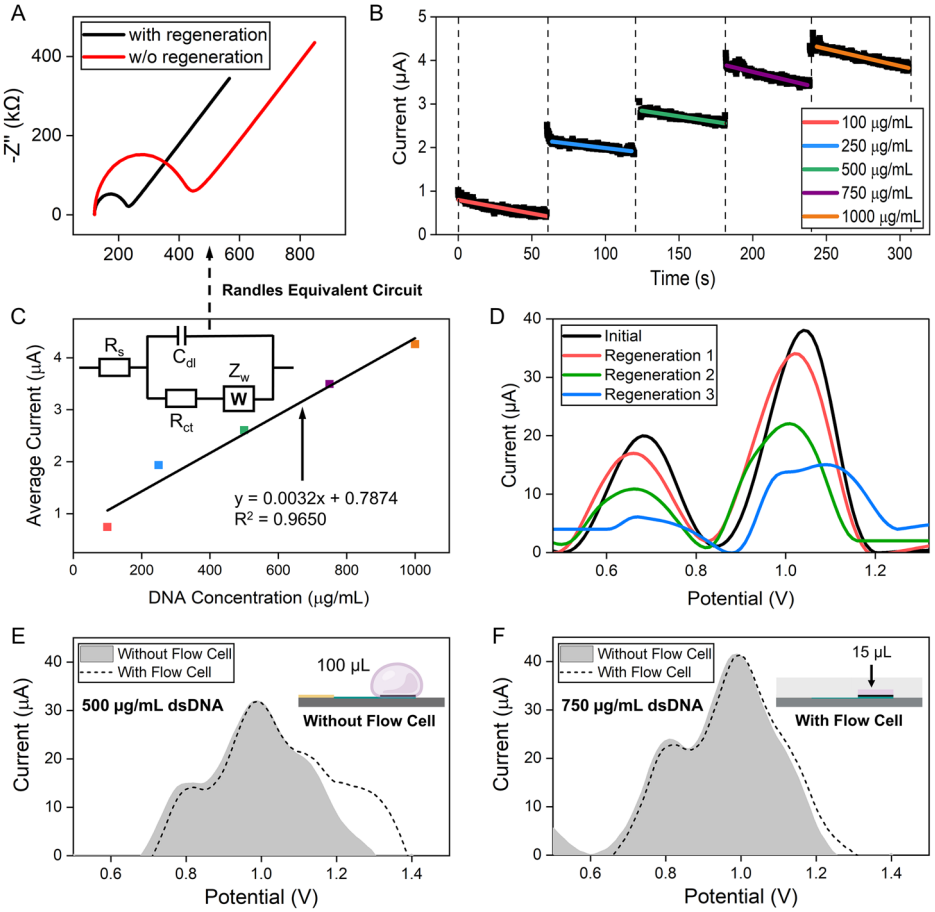


Fig. 3 | Electrochemical characterization and low-volume dsDNA detection using the integrated platform. A Nyquist plot of the activated SPE (black line) and the non-activated SPE (red line) obtained in a solution containing 10 mM $K_4[Fe(CN)_6]/K_3[Fe(CN)_6]$ and 0.1 M KCl. **B** Chronoamperometric current-time responses obtained after sequential injection of dsDNA solutions at increasing concentrations (100–1000 μg/mL) onto the SPE surface via the flow cell, demonstrating concentration-dependent current variations. **C** Calibration curve obtained from chronoamperometry measurements, showing the linear relationship between dsDNA concentration and the average current response. Inset: Randles equivalent circuit model for the EIS analyses. **D** Results of the regeneration experiments demonstrated the reusability of the electrodes, where the regeneration process was applied three times on the electrode surface. DPV responses obtained for (**E**) 500 and **F** 750 μg/mL dsDNA, showing that only ~15 μL sample was required with the flow cell (dashed line), compared to 100 μL without a flow cell (gray). Created with BioRender.com.

dsDNA solutions at concentrations of 100, 250, 500, 750, and 1000 μg/mL were sequentially injected onto the electrode surface via the microfluidic pumping module (60 s each, at 0.5 mL/min), enabling precise temporal control and minimizing user-induced variability. The resulting current-time traces depicted in Fig. 3B revealed clear concentration-dependent increases in steady-state current. Here, the resulting current-time responses reflect the electron-transfer processes associated with DNA adsorption and interaction at the electrode interface. Short pauses were included between injections to allow the previous bolus to diffuse away from the electrode surface and to re-establish the baseline, thereby minimizing carryover effects. To further enhance data clarity, the raw signals were processed using a Fast Fourier Transform (FFT) filter, suppressing background noise and improving the signal-to-noise ratio. In addition, smoothing was performed using a low-pass parabolic filter with a cutoff frequency of 10 Hz and a window size of 5 points, which further reduced signal fluctuations and facilitated clearer data interpretation[45]. Chronoamperometric measurements demonstrated that increasing dsDNA concentrations yielded proportionally higher current responses.

As shown in Fig. 3C, a linear relationship was obtained, e.g., $I = 0.0032C + 0.7874$, over the range of 100–1000 μg/mL, with a correlation coefficient of $R^2 = 0.9650$. In the equation, $I(\mu A)$ is the steady-state current extracted from the chronoamperometry traces and $C(\mu g/mL)$ is the dsDNA concentration of the injected solution. The slope of 3.2 nA/(μg/mL) indicates the sensitivity of the system. The low standard deviation across replicates confirmed high measurement reproducibility, underscoring the reliability of the integrated microfluidic delivery and detection approach. These findings also confirm that the pump-driven delivery and electrochemical readout operated in synchrony within the flow-cell platform, ensuring both precision and reliability.

Reusability of SPEs via regeneration process

SPEs are typically designed for single-use applications; however, their limited reusability can be exploited through an appropriate regeneration strategy. In this study, we implemented a regeneration protocol involving the application of +1.8 V for 60 seconds in acetate buffer (ACB, pH 4.8), applied both as a pre-conditioning activation step and as a regeneration treatment following electrochemical measurements. In all experiments, electrodes were first subjected to this activation step to enhance their electrochemical activity prior to analysis. This pre-conditioning treatment increased the density of electrochemically active sites, promoted electron-transfer kinetics, and improved the affinity of the carbon electrode surface for dsDNA adsorption. These improvements are mostly associated with enhanced surface hydrophilicity, the introduction of additional carbon-oxygen functional groups on the SPE surface[46], increased surface roughness[47], and the removal of organic residues or contaminants originating from the printing process. After activation, each electrode was incubated with 500 μg/mL dsDNA for 45 min at room temperature and analyzed in ACB using the DPV. In these DPV scans (+ 0.4 to +1.4 V vs Ag/AgCl), two oxidation peaks are reproducibly observed, and assigned to guanine (~0.8–0.9 V) and adenine (~1.0–1.2 V) on the activated carbon surface; pyrimidine (T/C) oxidation typically occurs at higher overpotentials with much lower currents on carbon and is therefore not resolved under our window and pulse settings[48]. This constituted the initial measurement. Following the initial measurement, the electrodes were subjected to the regeneration protocol, again applying +1.8 V for 60 seconds in ACB. After regeneration, the same incubation and measurement procedure was repeated, and the resulting response was recorded as the first regeneration measurement. We repeated the regeneration-measurement cycle twice more to obtain the second and third responses (Fig. 3D); only the first regeneration preserves similar peak structure with lower amplitude, the

second yields reduced yet usable signals for qualitative screening, and the third shows substantial broadening/attenuation that limits quantitative use. Across these cycles, both the guanine and adenine peaks attenuate and broaden, consistent with progressive surface oxidation and loss of electroactive sites.

The impact of repeated regenerations was quantified using the signal loss formula, e.g., $Signal\ Loss(\%) = 100 \times (I_0 - I)/I_0$. In this equation, where I_0 is the peak current measured before regeneration, and I is the current after each regeneration cycle, both at the same potential, e.g., for the adenine peak at +1.0 V. Taking $I_0 = 37.00$ μA, the signal losses were calculated as 9.5%, 43.2%, and 64.9% after the first, second, and third regenerations, respectively. Results indicate that regeneration effectively restores activity short term, but repeated cycles damage the SPE's carbon structure through irreversible oxidation and pathway disruption, reducing active sites and hindering electron transfer. A single regeneration cycle can reduce costs, but repeated use degrades performance, underscoring the trade-off between sustainability and reliability in flow-cell biosensing.

Low-volume electroanalysis using flow-cell delivery

One of the critical advantages of the flow-cell platform is its ability to perform electrochemical assays using significantly smaller sample volumes without compromising analytical performance. Traditional pipetting-based approaches often require ≥100 μL of biological or chemical samples, which may be impractical or costly in applications involving precious or limited-volume analytes. In contrast, our flow-cell system enables efficient sample delivery and electrochemical readout using as little as ~15 μL, making it ideal for resource-constrained or point-of-care settings. To illustrate this, DPV signals from the conventional drop-cast method were compared with flow-cell delivery to assess whether controlled microfluidic handling improves reproducibility, enhances signal magnitude, and reduces sample volume. For this assessment, calf thymus dsDNA was tested at concentrations of 500 and 750 μg/mL. At 500 μg/mL, both delivery formats produced two oxidation peaks near ~0.80 V and ~1.00 V (Fig. 3E). In the pipette-based format (gray curves), the mean peak currents were 7.47 ± 0.32 μA and 27.37 ± 0.55 μA, while the flow-cell configuration (black dashed lines) yielded 8.33 ± 2.15 μA and 27.21 ± 1.90 μA for the corresponding peaks. At the higher concentration of 750 μg/mL (Fig. 3F), the guanine oxidation peak (~1.0 V) reached 45.15 ± 4.86 μA in the pipetted format, whereas the flow-cell system produced a notably stronger and more consistent signal of 52.05 ± 2.30 μA. These results confirm that the flow-cell system not only provides comparable or enhanced signal intensities but also improves reproducibility, particularly at higher analyte concentrations. Importantly, this enhancement is achieved while reducing the required sample volume from ~100 μL to just ~15 μL per measurement. The improved performance can be attributed to more uniform analyte distribution, minimized evaporation, and enhanced analyte delivery under continuous flow conditions. Additionally, the peak potential remained consistent across formats, indicating that the observed benefits stem from improved delivery mechanics rather than electrochemical shifts. Overall, this comparative analysis underscores the superior efficiency and analytical robustness of the flow-cell platform, validating its use as the preferred configuration for low-volume, high-precision electrochemical biosensing applications.

In this section, dsDNA was intentionally selected as a simple, well-characterized model analyte to benchmark the engineering and workflow performance of the proposed platform rather than to establish a new or highly optimized nucleic acid sensing chemistry. The objective of this study is not to compete with ultra-low-volume or mass-sensitive detection technologies, such as FET-based electronic biosensors, which prioritize absolute sensitivity through specialized device physics. Instead, the present system emphasizes reproducible low-volume operation, defined contact volume control, automated delivery–measurement sequencing, and reduced operator dependence using off-the-shelf SPEs and low-cost components. The observed improvements in variability, baseline stability, carryover, and hands-on time therefore reflect system-level workflow advantages uniquely enabled by the integrated closed-loop microfluidic architecture. In this context, the dsDNA assay serves as a functional benchmark to validate platform robustness and quantitative consistency under flow rather than as a demonstration of state-of-the-art detection limits.

Graphical user interface

The graphical user interface (GUI) of the platform was developed in C# using Microsoft Visual Studio and designed as a comprehensive environment that integrates hardware control, data acquisition, chemical solution calculations, and advanced data analysis. Figure 4A shows the main panel of the GUI, providing the operator with control over the hardware components of the microfluidic and measurement modalities. For detailed views of each functional panel, refer to Supplementary Figs. S1– S14. In the "Connection" panel, the green arrow icon allows the system to scan and list all potentiostats connected to the computer. Once a potentiostat is successfully connected, the connection status indicator is updated accordingly, and the "Connect" button automatically switches to "Disconnect". The connection is managed through the PalmSens4 Software Development Kit (SDK), which has been integrated into the GUI to ensure smooth execution of electrochemical measurements. The communication protocol between the GUI and the potentiostat is established via serial communication or Bluetooth, providing reliable and fast data transfer.

The "Calculator" panel comprises four modules, including ppm calculator, solution dilution, gram-to-mole converter, and pH-pOH calculator that assist operators in performing routine solution calculations with accuracy. When the "ppm Calculator" panel is selected, the operator can input either the molarity (M) or molar mass (M_n) to obtain the corresponding ppm value, or directly enter ppm to calculate molarity using the following equation, $M = (ppm \times 0.001)/M_n$. This allows rapid conversion between commonly used concentration units without manual calculation. In "Solution Dilution Module" panel, operators can prepare working solutions from concentrated stocks through the classical relation, $C_1V_1 = C_2V_2$. After defining three of the four parameters (stock concentration C_1, stock volume V_1, final concentration C_2, and final volume V_2), the calculator automatically computes the desired value. This function ensures accurate and reproducible preparation of diluted solutions for experimental assays. In the "Gram to Mole Calculator" panel, users can calculate the number of moles (n) from a given mass (m) and molar mass (M) via the following equation, $n = m/M$, or determine the required mass for a specified number of moles using the following equation, $m = n \times M$.

A built-in compound library allows users to select a chemical directly, automatically filling the molar mass field for convenience. A "Reset" button is available to clear all entries and return the panel to default settings. The "pH - pOH Calculator" panel is designed to determine the acidity or alkalinity of a solution. The concentration of hydronium ions (H_3O^+) is used to calculate the pH value according to the formula $pH = -\log[H_3O^+]$. If the solution is basic, the concentration of OH^- ions is determined based on the given molarity. The pOH is then calculated using the formula $pOH = -\log[OH^-]$, and the pH value is obtained by subtracting this result from the upper limit of the pH scale, 14.

The "Regeneration Process Panel" is designed to extend the usability of SPEs through the application of controlled electrical potentials. In this panel, the operator specifies two parameters: the potential (V) to be applied and the duration (s). The regeneration procedure is activated by pressing the "Start" button. This process restores electrode activity, enabling previously used SPEs to be cleaned and reliably reused. The "Console" panel provides a detailed log of the device's communication and operational events in real-time. It continuously records system messages such as device detection, successful connections, disconnections, and error notifications, allowing the operator to track all interactions between the GUI and the potentiostat. For example, when a potentiostat is recognized, the console displays messages, e.g., "Found 1 device(s)", and upon establishing a connection, it confirms with "Connected to PalmSens4". During measurements, the console also reports instantaneous values of potential (V) and current (A), along with the overall device status, e.g., Idle, Running.

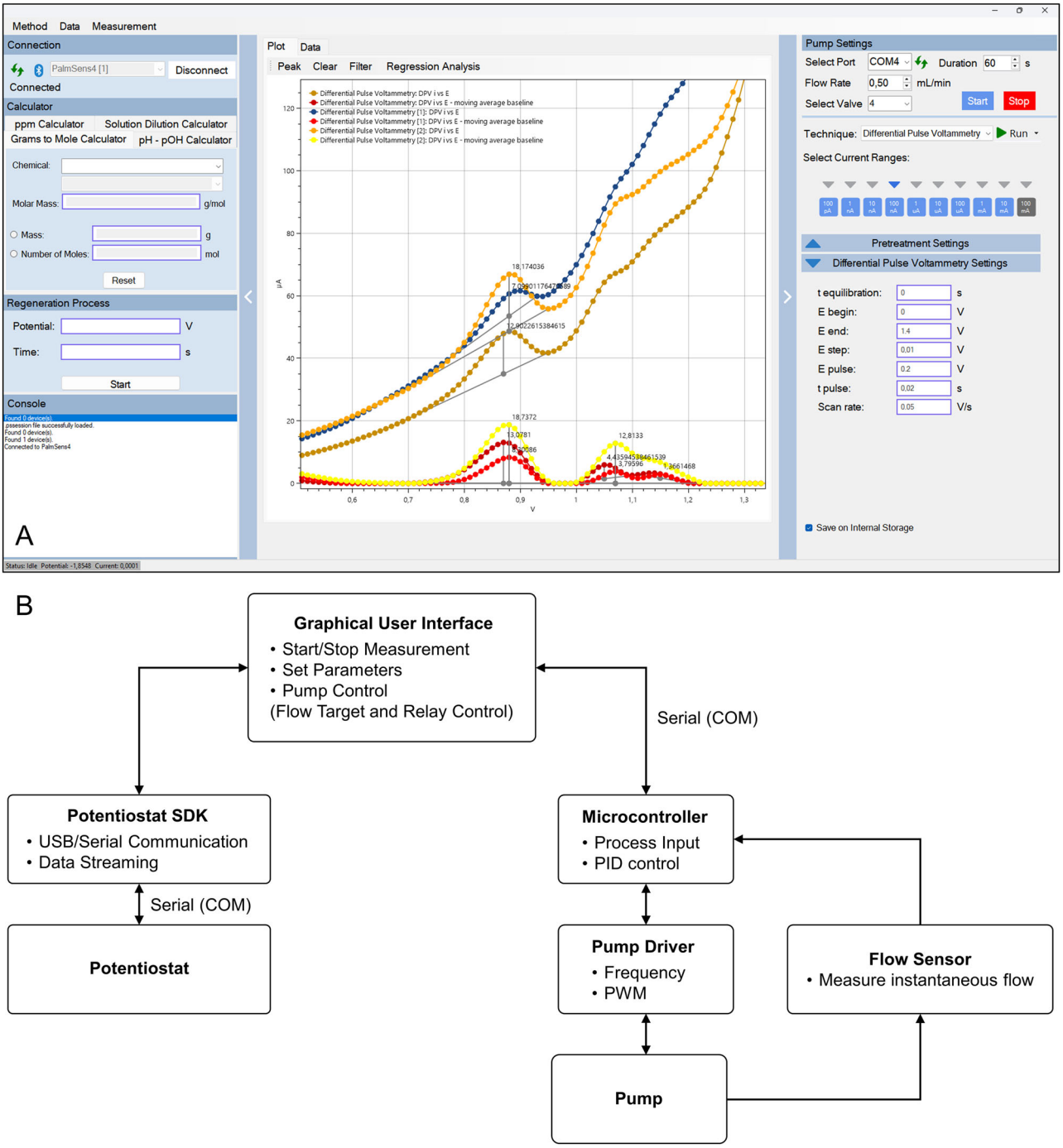


Fig. 4 | Software architecture and control interface of the integrated electrochemical platform. A Main menu of the system GUI. **B** Block diagram of data-flow and control.

At the center of the GUI, acquired measurements are displayed as two-dimensional graphs, with the corresponding data accessible to the operator. This panel consists of two main sections: "Plot" and "Data". The Plot section provides a comprehensive visualization of electrochemical measurements by representing CA as current-time plots, DPV, and CV as potential-current curves. The "Data" section presents the corresponding measurement values in a structured tabular format, with each entry identified by a unique ID number. This dual representation enables users to examine their electrochemical results both graphically and numerically.

Real-time current-potential curves are rendered using the WinForms graphics library in combination with the psCommSimpleForms component, allowing users to visualize electrochemical responses immediately after acquisition. Tabulated outputs are managed through the WinForms.DataGridView element, ensuring that numerical results are displayed in a clear and organized manner. Additionally, the panel integrates a "Peak" subgroup with options such as "Smooth Curve", "Average Baseline", "Subtract Baseline", and "Detect Peaks", implemented using the PalmSens SimpleCurve class. These tools support advanced data processing tailored to experimental needs, e.g., smoothing provides clearer visual outputs, baseline averaging and subtraction isolate meaningful signal responses, and peak detection identifies peaks with precision. Complementary functions, such as the "Clear" option, allow users to remove all displayed curves, while the "Filter" button enables the selection of specific peaks or datasets for further analysis.

The "Regression Analysis" panel enables users to process electrochemical measurement data and generate calibration curves by applying linear regression. On the left-hand side, all available measurement curves (e.g., DPV curves) are listed in the "Curves" panel, and the operator can select which datasets to include in the analysis. For each selected curve, the associated concentration (e.g., mg/mL) and current (e.g., mA) values are displayed and can also be entered manually through the "Manual Peak Input" section. This flexibility allows additional data points to be incorporated beyond automatically extracted peaks. Once the desired datasets are defined, pressing the "Analysis" button initiates linear regression, resulting in the calculation of the regression equation $\left(y = ax + b\right)$, the coefficient of determination (R^2), as well as analytical performance metrics such as the limit of detection (*LOD*) and limit of quantification (*LOQ*). The right-hand side of the panel graphically displays the regression results, where experimental data points appear as black markers and the fitted regression line is shown as a red dashed line. Numerical outputs including slope, intercept, LOD, LOQ, and R^2 are displayed below the graph, providing quantitative insight into sensor performance. LOD and LOQ are calculated according to standard analytical chemistry formulas, where $LOD = 3.3 \times (\sigma/m)$ and $LOQ = 10 \times (\sigma/m)$, with σ representing the standard deviation of residuals and m the slope of the regression line.

The "Pump Settings" panel provides the operator with precise control over the microfluidic flow system by allowing manual configuration of pump parameters. In this panel, the "Select Port" dropdown menu is used to specify the serial port of the microcontroller controlling the pump, with the refresh icon enabling re-scanning of available ports. The "Duration" (s) field defines the total time for which the pump will operate, while the "Flow Rate" field sets the volumetric delivery rate in mL/min. The "Select Valve" menu allows the operator to choose the active valve channel for directing fluid flow. Once parameters are set, pressing the "Start" button initiates pump operation according to the specified flow rate and duration, and pressing the "Stop" button terminates the process immediately. This functionality enables the operator to manually run the pumps either to deliver a defined solution volume or to maintain a constant flow for a specified duration, ensuring flexibility and precision in fluid handling during experiments. Furthermore, the operator can choose to keep the flow continuous during measurements or stop the pump module after introducing the analyte onto the electrode surface, allowing measurements to be carried out under static conditions.

The "Technique" panel located at the right-hand side of the GUI enables the operator to select the electrochemical technique, define the applicable current range, and configure technique-specific parameters prior to initiating an experiment. This panel allows users to choose among commonly used electrochemical methods such as CV, DPV, and CA, as well as additional techniques supported by the system. The "Select Current Ranges" section defines the operational current window of the potentiostat, directly affecting measurement sensitivity and dynamic range. Once the desired technique and parameters are entered by the operator, the experiment is initiated by pressing the "Run" button, which triggers automated execution of the selected measurement protocol. At the end of a measurement, the operator can save the selected technique and the corresponding input parameters. The GUI supports exporting results in both Excel (.xlsx) and PalmSens session (.pssession) formats, and it is capable of reloading these files.

System architecture and communication structure

GUI manages both the electrochemical measurements and the microfluidic control units. The system operates through two independent communication channels, e.g., (i) potentiostat communication channel and (ii) microcontroller communication channel. Communication with the potentiostat is established via the manufacturer software development kit (SDK). The Palmsens SDK exposes a high-level API in C# for device initialization, measurement parameter definition, and measurement execution. Current-potential (I-E) data are streamed to the GUI in real-time through the SDK's event-driven callbacks and are simultaneously visualized, enabling uninterrupted acquisition, display, and analysis during measurements.

The second channel interfaces with the microcontroller-based pump control system (Bartels Mikrotechnik MP6-QuadOEM). The microcontroller drives the piezoelectric pump via the I2C protocol while reading real-time flow-rate data from the flow sensor (Sensirion SLF3C-1300F). The firmware implements a PID controller that dynamically adjusts pump frequency and pulse-width modulation (PWM) amplitude to maintain the target flow rate. Serial commands from the GUI follow the ASCII format "flow, relay", e.g., "0.7,2" sets the target flow rate to 0.7 and activates relay 2, and "0,0" stops the pump. Integral anti-windup and output-smoothing mechanisms are included to prevent rapid fluctuations in the control signal. The microcontroller communicates with the GUI over a dedicated serial (COM) port, independent of the potentiostat channel, and processes incoming commands at the hardware level to control relays, pump frequency, and PWM amplitude accordingly.

Discussion

This study demonstrates the successful development of an integrated electrochemical sensing platform that combines a custom-designed 3D-printed flow cell, a microfluidic pumping module, and a dedicated C#-based GUI. The proposed platform overcomes several limitations commonly associated with conventional SPE-based systems, including manual sample handling, unregulated fluid dynamics, and reliance on proprietary external software. Instead, it provides a compact, low-cost, and automated solution for high-performance electrochemical biosensing. The experimental results clearly show that the system enables reliable, low-volume analysis with a sample requirement of only ~15 µL per measurement. CA experiments performed with dsDNA targets revealed a linear correlation between concentration and current response, confirming the quantitative capability of the platform under serial-injection conditions. The present configuration demonstrates label-free electrochemical differentiation under low-volume, closed-loop flow. Comprehensive controls, e.g., ss vs. dsDNA, GC/length panels, interferents, pH/ionic strength, are out of scope for this platform-focused work, and will be pursued in follow-on, chemistry-specific studies employing target-specific recognition layers and antifouling strategies. Compared to traditional pipette-based delivery, the flow-cell configuration achieved comparable peak currents while utilizing significantly lower analyte volumes. To quantify the practical gains under matched conditions, we include a side-by-side benchmark of closed-loop flow versus pipetted delivery, summarizing improvements in variability, baseline drift, hands-on time, and carryover. Under matched conditions, closed-loop delivery yielded lower variability (CV~3% vs ~8%), reduced baseline drift, and shorter hands-on time, while achieving comparable signal with ~15 µL effective contact volume. Building on this, the closed-loop flow cell also decreased operator dependence by scripting delivery–measure–rinse sequences and stabilizing delivery, which translated to tighter replicate dispersion and lower operator-to-operator CV. Although total sample loaded per run is higher in the flow mode (~45 µL plug) than in static drops (~20 µL), the effective contact volume at the electrode is comparable (~15 µL) and the automation shortens hands-on time, aiding throughput and consistency. Baseline drift and carryover were both reduced under closed-loop control, consistent with steadier hydrodynamics and rapid valve-driven rinses. Overall, these results support the platform's claim of comparable signal with improved reproducibility and workflow efficiency relative to pipette-based delivery. As an additional note, matched conditions used the same SPE lot, buffer, potentiostat, and room temperature. "Effective contact volume" is the chamber volume (~15 µL) directly over the SPE; "total sample per run" includes the upstream plug used to maintain steady flow. Hands-on time was measured from sample placement/selection to measurement start; total time to result includes acquisition. This performance enhancement likely stems from more controlled analyte delivery, improved mass transfer, and reduced sample evaporation, emphasizing the benefits of integrating controlled fluidics into SPE-based sensing setups.

The dsDNA experiment serves as a functional benchmark of the platform's controlled-flow operation and quantitative readout rather than an attempt to minimize system LOD. The reported linear range and R^2 demonstrate that serial-injection, low-volume delivery supports robust calibration on SPEs. We did not optimize recognition chemistry or amplification, e.g., the present LOD reflects an engineering baseline. In applications prioritizing maximal sensitivity, the same hardware can be paired with target-specific surfaces (intercalator-assisted voltammetry, redox-labeled probes, aptamer monolayers, or enzymatic amplification) and flow-assisted preconcentration, which are expected to lower LOD and extend dynamic range. Thus, the platform is intended as a general, low-volume SPE chassis on which assay-specific chemistries can be layered to reach application-dependent performance targets. Relative to prior "all-in-one/automated" platforms, our approach targets a different objective and operating regime: benchtop, low-volume molecular biosensing on SPEs with closed-loop, programmable serial injections and head-to-head delivery benchmarking (flow versus pipette).

Prior exemplars include a smartphone-mediated, self-powered CRISPR/nanozyme chip for miRNA-141 (visual + electrochemical readout)[49], an all-in-one salivary cotinine device that couples a cotton-swab collector to a fixed-volume microfluidic immunosensor[50], and an organic electrochemical transceiver that integrates sensing with triggered release for intelligent wearables[51]. In contrast, the present work targets benchtop molecular biosensing on SPEs with closed-loop, programmable serial injections (~15 µL), a head-to-head flow-versus-pipette study, and quantified SPE regeneration-capabilities not demonstrated in these prior systems.

Another key strength of this work is the low fabrication cost of the flow cell, approximately $6, substantially lower than commercially available SPE-compatible flow cells. This cost efficiency enhances the platform's feasibility in resource-constrained settings or point-of-care environments. Importantly, the platform also enables partial regeneration and reuse of the SPE. After a single regeneration cycle, ~90.5% of the original signal was retained, indicating the feasibility of reusing the electrode with minimal performance loss. However, repeated regeneration cycles led to progressively reduced signal intensities, highlighting the need for further optimization of regeneration protocols or the development of more robust electrode surfaces to support extended reuse. Practically, regeneration should be viewed as limited reuse, e.g., the first cycle preserves similar peak structure at lower amplitude, a second cycle yields reduced but qualitatively usable signals, and additional cycles exhibit substantial attenuation/broadening.

The custom-developed GUI substantially strengthens the innovation of this platform by integrating hardware control, solution-specific calculators, advanced data analysis, and real-time signal visualization in a single software interface. This integration reduces reliance on third-party tools, improves reproducibility, and simplifies user operation. Built-in tools for regression analysis, LOD/LOQ calculation, and customizable plotting make the system highly accessible even to users with limited electrochemical expertise.

Despite these advances, several limitations merit note. Validation was performed with dsDNA in buffer; performance in complex biofluids (serum, saliva, urine) still needs systematic study for matrix effects and fouling. The reported calibration window (100–1000 µg/mL) and LOD/LOQ were not optimized for trace targets, e.g., achieving lower limits will require target-specific surfaces and/or amplification. SPE-to-SPE and lot variability can affect responses; while a single regeneration retained ~90.5% of the initial signal, additional cycles degraded performance, so single-use or limited reuse is advisable for critical assays until more robust surfaces are available. Closed-loop stability may be perturbed by bubbles, tubing compliance, or temperature-dependent viscosity; bubble traps/degassing, tighter tubing tolerances, and optional temperature control can mitigate this. Mechanical tolerances (gasket compression, SPE alignment) and residual dead volume may contribute to carryover; future designs will quantify dead volume and add alignment fixtures. SLA resin biocompatibility/solvent tolerance/sterilization may restrict some assays, motivating alternative materials or coatings. Finally, portability (battery operation, wireless connectivity) and field robustness, software maintenance (versioning/updates), and operator training (SOPs) all require further work. Results also generalize from a single model analyte and short-term trials; broader analyte classes and longer-term drift/ruggedness with blinded, inter-operator studies remain as next steps.

For translation to real samples, the four-line valve manifold enables a matrix-aware script: (i) Sample (e.g., 1:1–1:10 dilution in ACB to normalize pH/ionic strength), (ii) Conditioning-binding buffer to stabilize adsorption, (iii) Targeted rinses (brief low-flow washes; optional 0.01–0.05% Tween-20 or high-salt to reduce nonspecific adsorption), and (iv) Regeneration/blank for baseline subtraction as needed. Matrix-matched calibration or standard addition can correct residual matrix effects; spike-and-recovery at low/medium/high levels (targeting ~80 - 120% recovery with ≤15% CV) plus intra- or inter-operator replicates will quantify accuracy and robustness. Practical safeguards include inline bubble traps, closed-loop control to hold setpoints despite viscosity changes, optional reference cycles (matrix without analyte), and antifouling/pretreatments (e.g., BSA/CASE, dilute Nafion, or zwitterionic coatings) alongside short adsorption windows and gentle rinses.

Looking forward, the proposed platform establishes a foundation for several future research directions. These include integration of multiplexed SPE arrays for simultaneous multi-analyte detection, coupling with target-specific biorecognition layers such as aptamers or antibodies for clinical biomarkers, miniaturization toward battery-powered and handheld formats, and incorporation of wireless or smartphone-based interfaces for field deployment. In addition, combining the closed-loop fluidics with automated calibration routines, AI-assisted signal processing, and standardized open-source hardware designs could further enhance robustness, scalability, and accessibility. Collectively, these developments position the system as a versatile chassis that can evolve from a laboratory prototyping tool into a broadly deployable point-of-care and environmental diagnostic platform. In order, to contextualize the platform's positioning and guide future work, we provide a concise SWOT analysis of the proposed system (Table 2).

Future work will miniaturize the pump for portability, validate performance in complex biological and clinical samples, and assess long-term stability. Planned improvements include multiplexing, wireless/smartphone connectivity, and AI-driven signal processing, advancing the platform toward an autonomous, user-friendly diagnostic tool for point-of-care and field use (Table 3).

Table 2 | SWOT analysis of the integrated microfluidic-electrochemical platform

Factor	Points to note
Strengths	Integrated, closed-loop microfluidics; unified GUI (control + analysis); ~15 µL per run; low fabrication cost; documented single-cycle regeneration.
Weaknesses	Tested mainly with dsDNA in buffer; calibration window (100–1000 µg/mL) not tuned for trace detection; multi-cycle regeneration losses; sensitivity to bubbles/alignment/dead volume.
Opportunities	Complex-matrix validation; multiplexing; improved surfaces/materials; portable/battery operation; wireless/phone UI; broader community uptake via open designs.
Threats	SPE lot/vendor variability; resin/sterilization constraints; strong commercial incumbents; software maintenance and training needs.

Table 3 | List of Abbreviations

Abbreviation	Definition
ACB	Acetate Buffer
CA	Chronoamperometry
CAD	Computer-Aided Design
CE	Counter Electrode
CFD	Computational Fluid Dynamics
CV	Cyclic Voltammetry
DI	Deionized
DPV	Differential Pulse Voltammetry
dsDNA	Double-Stranded DNA
EIS	Electrochemical Impedance Spectroscopy
FEM	Finite Element Method
FFT	Fast Fourier Transform
GUI	Graphical User Interface
I–E	Current–Potential
IPA	Isopropyl Alcohol
LOD	Limit of Detection
LOQ	Limit of Quantification
PDMS	Polydimethylsiloxane
PID	Proportional–Integral–Derivative
PWM	Pulse Width Modulation
RE	Reference Electrode
R^2	Coefficient of Determination
Rct	Charge Transfer Resistance
SDK	Software Development Kit
SLA	Stereolithography
SPE	Screen-Printed Electrode
SPCE	Screen-Printed Carbon Electrode
SWOT	Strengths, Weaknesses, Opportunities, Threats
WE	Working Electrode

In conclusion, we presented a compact, low-cost, and fully integrated electrochemical platform that unites a custom 3D-printed flow cell, a closed-loop microfluidic pumping module with PID-regulated pumping, and a C#-based GUI for instrument control and real-time analysis. The system enables reliable low-volume operation (~15 µL per measurement) and delivers quantitative performance using dsDNA as a model analyte, with chronoamperometric calibration linearity across 100–1000 µg/mL ($R^2 \approx 0.965$). Relative to pipette-based delivery, flow-cell DPV measurements achieved comparable peak responses with enhanced reproducibility while consuming markedly less sample. We further demonstrated practical SPE reuse via an on-board electrochemical regeneration step, retaining ~90.5% of the initial signal after a single cycle, thereby defining realistic reuse limits. The flow cell's ~$6 fabrication cost and use of off-the-shelf components support broad accessibility and rapid adoption. Compared with alternative ultra-low-volume or chemistry-specialized microfluidic systems, the present platform emphasizes accessibility, low fabrication cost, and assay generality, trading extreme volume minimization or assay-specific optimization for reproducible, automated operation using off-the-shelf SPEs. Overall, the results point to a feasible, integrated approach for SPE assays that may streamline workflows and improve consistency. Further studies will be needed to assess multiplexed measurements and to explore applicability in point-of-care and field contexts. Future work will also extend testing to complex biological and environmental matrices using matrix-matched calibration and spike-and-recovery protocols to demonstrate accuracy and precision under application-relevant conditions.

Methods

Flow cell fabrication

Rigid clear resin (FLGPCL41, Formlabs Inc., USA) was employed in the fabrication of the bottom and top covers, which constitute the main body of the flow cell. Following this fabrication process, internal microchannels were flushed with isopropyl alcohol (IPA, Sigma-Aldrich) under pressure using a syringe to ensure the removal of uncured resin residues. Subsequently, the printed parts were immersed in IPA for 25 min using a Form Wash unit and thoroughly air-dried. Final curing was carried out in a Form Cure station by exposing the components to UV light at 365 and 400 nm at 60 °C for 45 min. The O-ring was fabricated using elastic resin (FLELCL02, Formlabs Inc., USA). Post-fabrication, the O-ring was washed for 15 min and UV-cured at 70 °C for 30 min, achieving optimal elasticity and sealing performance. A 3 mm-thick PDMS (polydimethylsiloxane) support layer was fabricated for electrode placement. The mold for this purpose was 3D-printed using clear resin, then filled with a 10:1 mixture of PDMS base and curing agent (SYLGARD™ 184 Silicone Elastomer Kit, 001004673804, Dow, USA). The PDMS mixture was degassed in a desiccator (ISOLAB Laborgeräte GmbH) and cured at 70 °C for at least 1 h, forming a soft interface to cushion the SPE and enhance mechanical integration. In the final assembly, the SPE is sandwiched between the resin covers, which are fastened together with screws and nuts on each side. The supporting PDMS layer is positioned on the inner surface of the bottom cover, while the O-ring is integrated into the top cover to ensure proper sealing. A step-by-step schematic and photographic illustration of the complete fabrication and assembly workflow is provided in Supplementary Fig. 15 to visually document the manufacturing process and facilitate reproducibility of the device.

Chemicals, buffers, and instruments

Electrochemical measurements were performed using a portable potentiostat (PalmSens4, PalmSens®). The acetate buffer (ACB, pH 4.8) was prepared using 0.5 M glacial acetic acid (695092, Sigma-Aldrich, Germany) and 20 mM sodium chloride (NaCl, S9888, Sigma-Aldrich, Germany). Screen-printed carbon electrodes (SPCEs, DRP-110, Spain) were purchased from Metrohm DropSens. DNA quantification and purity assessment were performed using a NanoDrop 2000 spectrophotometer (Thermo Scientific™). A laser engraver (Epilog Legend Mini 24, Epilog Laser) was used to cut acrylic components for platform housing. PDMS layers were prepared using the Silicone Elastomer Kit (Dowsil SYLGARD™) at a 10:1 base-to-curing agent ratio. Flow cell components and supporting holders were fabricated using an SLA-based 3D printer (Formlabs Form 3).

Electrochemical measurements

To activate the electrode surface and enhance electrochemical performance, each SPE was activated in ACB (pH 4.8) by applying the potential at +1.8 V for 60 s. Ultrapure water (resistivity ≥18 MΩ·cm) prepared with a water purification system (Millipore) was used in all assays and solutions. DPV measurements were performed in the range between +0.4 V and +1.4 V, with a potential step of 0.01 V, a pulse amplitude of 0.2 V, and a pulse duration of 0.02 s. The scan rate was set to 0.05 V/s. CA measurements were carried out with a 10-second equilibrium time, an applied potential of 0.85 V, a measurement interval of 0.1 s, and a total measurement time of 600 s. All measurements were conducted at room temperature.

Prior to measurement, anodic activation increases edge-plane density and introduces oxygen-containing groups on the carbon SPE, enhancing nucleic-acid adsorption and electron-transfer kinetics. During the pre-accumulation/injection step, dsDNA adsorbs onto the working electrode predominantly via π-π interactions between nucleobases and sp^2-carbon domains, aided by ionic-strength-screened interactions of the phosphate backbone. At the fixed CA potential of +0.85 V vs Ag/AgCl, the faradaic response is dominated by guanine oxidation of surface-adsorbed dsDNA; adenine typically oxidizes at higher potentials (> 1.0–1.1 V on carbon), with pyrimidines higher still, making their contribution at +0.85 V negligible under our conditions. Accordingly, the CA signal at +0.85 V tracks the surface coverage of guanine-containing dsDNA delivered by the serial-injection workflow.

CFD simulation based on FEM

CFD simulations based on the Finite Element Method (FEM) were performed using COMSOL Multiphysics version 6.3 to investigate the steady-state laminar flow characteristics inherent in the electrochemical cell configuration. The working fluid was defined as incompressible and Newtonian, with a density of 1000 kg/m^3 and a dynamic viscosity of 0.99 cP (0.00099 Pa·s), respectively. All interior channel surfaces were subject to a no-slip boundary condition. The inlet boundary conditions were defined by volumetric flow rates of 0.2, 0.3, 0.4, 0.5, and 0.6 mL/min, translating to volumetric flow rates between 3.33×10^{-9} and 1.00×10^{-8} m^3/s. These volumetric flow rates yielded average inlet velocities that varied from approximately 0.0013 to 0.0039 m/s, as determined from the cross-sectional area of the channel. The outlet boundary condition was established at zero-gauge pressure. The Reynolds number was calculated using the channel's hydraulic diameter of 1.8 mm to determine the laminar flow regimes. The resultant values fluctuated between 2.4 and 7.2 across all experimental conditions, remaining significantly below the transitional threshold, thereby confirming the presence of laminar flow. The incompressible Navier-Stokes equations governed the flow dynamics, while the transport phenomena of diluted electrochemical species were modeled using the convection-diffusion equation.

dsDNA experiment

A stock solution of calf thymus 5 mg/mL dsDNA (D8515, Sigma-Aldrich, Germany) was prepared in DI water and serially diluted to concentrations of 100, 250, 500, 750, and 1000 µg/mL. SPEs were pre-activated in ACB (pH 4.8) by applying +1.8 V for 60 s. CA measurements were carried out in a flow cell by sequentially injecting dsDNA solutions using a software-controlled pump (60 s per injection, 0.5 mL/min). Short pauses were introduced between injections to restore the baseline, and current-time responses were recorded for each concentration.

For reusability studies, SPEs were first activated in ACB at +1.8 V for 60 s, and then incubated with 500 µg/mL dsDNA for 45 min at room temperature. After rinsing with ACB, electrodes were analyzed by DPV to obtain the initial signal. Electrodes were regenerated by reapplying +1.8 V for 60 s in ACB, followed by the same incubation and measurement procedure. This regeneration-measurement cycle was repeated three times, and the responses obtained after each regeneration were compared with the initial measurement. To compare pipette-based and flow-cell delivery formats, dsDNA solutions at 500 and 750 µg/mL were tested. For the pipetted format, 100 µL of solution was directly applied to the SPE surface. For the flow-cell format, approximately 15 µL of dsDNA solution was delivered across the electrode surface using the pump system. All electrodes were incubated for 45 min at room temperature, rinsed with ACB (pH 4.8), and analyzed by DPV. Signal intensities and reproducibility between the two delivery formats were then evaluated.

Data availability

The datasets generated and/or analyzed during the current study are not publicly available due to intellectual property considerations related to the device design and associated software (including potential patenting/commercialization activities), but are available from the corresponding author on reasonable request. The following resources accompany this work: (i) CAD and print-ready STL files for the flow cell and fixtures; (ii) Circuit diagram and wiring schematic, (iii) Embedded firmware and the C# GUI source with compiled release, and (v) Example raw datasets (calibration/replicates) and figure-generation scripts.

Received: 22 September 2025; Accepted: 12 February 2026;
Published online: 02 March 2026

References

1. Harshita, Wu, H. & Kailasa, S. K. Recent advances in nanomaterials-based optical sensors for detection of various biomarkers (inorganic species, organic and biomolecules). *Luminescence* **38**, 954–998 (2023).
2. Saputra, H. A. Electrochemical sensors: basic principles, engineering, and state of the art. *Monatshefte f. ür. Chem. - Chem. Mon.* **154**, 1083–1100 (2023).
3. Alam, M. M., Mitea, V., Howlader, M. M. R., Selvaganapathy, P. R. & Deen, M. J. Analyzing electrochemical sensing fundamentals for health applications. *Adv. Sens. Res.* **3**, 2300100 (2024).
4. Guo, W. et al. DNA aptamer-based sensitive electrochemical biosensor for NAD(H) detection. *Biosens. Bioelectron.* **271**, 116996 (2025).
5. Peng, H.-L., Zhang, Y., Liu, H. & Gao, C. Flexible wearable electrochemical sensors based on AuNR/PEDOT:PSS for simultaneous monitoring of levodopa and uric acid in sweat. *ACS Sens.* **9**, 3296–3306 (2024).
6. Liu, Y. et al. ZnO-rGO-based electrochemical biosensor for the detection of organophosphorus pesticides. *Bioelectrochemistry* **156**, 108599 (2024).
7. Helim, R., Zazoua, A., Jaffrezic-Renault, N. & Korri-Youssoufi, H. Label free electrochemical sensors for Pb(II) detection based on hemicellulose extracted from Opuntia Ficus Indica cactus. *Talanta* **265**, 124784 (2023).
8. Periasamy, V. et al. Novel same-metal three electrode system for cyclic voltammetry studies. *RSC Adv.* **13**, 5744–5752 (2023).
9. Colburn, A. W., Levey, K. J., O'Hare, D. & Macpherson, J. V. Lifting the lid on the potentiostat: a beginner's guide to understanding electrochemical circuitry and practical operation. *Phys. Chem. Chem. Phys.* **23**, 8100–8117 (2021).
10. Abdullah, S., Tonello, S., Borghetti, M., Sardini, E. & Serpelloni, M. Potentiostats for protein biosensing: Design considerations and analysis on measurement characteristics. *J. Sens.* **2019**, 1–20 (2019).
11. Garrote, B. L., Santos, A. & Bueno, P. R. Perspectives on and precautions for the uses of electric spectroscopic methods in label-free biosensing applications. *ACS Sens.* **4**, 2216–2227 (2019).
12. Agnihotri, A. S. & Nidhin, M. Advanced electrochemical detection and profiling of the antihypertensive drug atenolol via a SPION-activated carbon nanocomposite interface. *Nanoscale Adv.* **7**, 4397–4411 (2025).
13. Madadelahi, M., Romero-Soto, F. O., Kumar, R., Tlaxcala, U. B. & Madou, M. J. Electrochemical sensors: Types, applications, and the novel impacts of vibration and fluid flow for microfluidic integration. *Biosens. Bioelectron.* **272**, 117099 (2025).
14. Baluta, S. et al. Differential pulse voltammetry and chronoamperometry as analytical tools for epinephrine detection using a tyrosinase-based electrochemical biosensor. *RSC Adv.* **12**, 25342–25353 (2022).
15. Lakhera, P. et al. Recent developments and fabrication of the different electrochemical biosensors based on modified screen printed and glassy carbon electrodes for the early diagnosis of diverse breast cancer biomarkers. *Mater. Today Chem.* **26**, 101129 (2022).
16. García-Miranda Ferrari, A., Rowley-Neale, S. J. & Banks, C. E. Screen-printed electrodes: Transitioning the laboratory in-to-the field. *Talanta Open* **3**, 100032 (2021).
17. Paimard, G., Ghasali, E. & Baeza, M. Screen-printed electrodes: Fabrication, modification, and biosensing applications. *Chemosensors* **11**, 113 (2023).
18. Amouzadeh Tabrizi, M. & Acedo, P. An electrochemical impedance spectroscopy-based aptasensor for the determination of SARS-CoV-2-RBD using a carbon nanofiber–gold nanocomposite modified screen-printed electrode. *Biosensors* **12**, 142 (2022).
19. Nazir, S. Advancing point-of-care testing with nanomaterials-based screen-printing electrodes. *Sens. Int* **6**, 100328 (2025).
20. Shen, Y. et al. Screen-printed electrodes as low-cost sensors for breast cancer biomarker detection. *Sensors* **24**, 5679 (2024).

21. Mincu, N.-B. et al. Screen-printed electrodes (SPE) for in vitro diagnostic purpose. *Diagnostics* **10**, 517 (2020).
22. Wang, K. et al. Nanochannel array on electrochemically polarized screen printed carbon electrode for rapid and sensitive electrochemical determination of clozapine in human whole blood. *Molecules* **27**, 2739 (2022).
23. Karthika, P., Shanmuganathan, S., Subramanian, V. & Delerue-Matos, C. Selective detection of salivary cortisol using screen-printed electrode coated with molecularly imprinted polymer. *Talanta* **272**, 125823 (2024).
24. Yu, Y. et al. Electrochemiluminescence drug detection with a nanoparticle-encapsulated luminophore on screen-printed electrodes. *Mater. Today Chem.* **29**, 101442 (2023).
25. Hassan, S. S. M., Kamel, A. H. & Fathy, M. A. A novel screen-printed potentiometric electrode with carbon nanotubes/polyaniline transducer and molecularly imprinted polymer for the determination of nalbuphine in pharmaceuticals and biological fluids. *Anal. Chim. Acta* **1227**, 340239 (2022).
26. Orzari, L. O. et al. Screen-printing vs additive manufacturing approaches: Recent aspects and trends involving the fabrication of electrochemical sensors. *Anal. Chem.* **97**, 1482–1494 (2025).
27. Moreno-Sibaja, F., Zou, D., Liu, S., Zhao, C.-X. & Gerstweiler, L. Microfluidics in biomanufacturing process development. *Biotechnol. Adv.* **85**, 108715 (2025).
28. Ferreira, M. et al. Advances in Microfluidic Systems and Numerical Modeling in Biomedical Applications: A Review. *Micromachines* **15**, 873 (2024).
29. Azagra, M. et al. Lab-on-a-chip metabolic analysis using benchtop NMR technology. *Anal. Chem*. **98**, 2701–2708 (2026).
30. Martinez, A. W., Phillips, S. T. & Whitesides, G. M. Three-dimensional microfluidic devices fabricated in layered paper and tape. *Proc. Natl. Acad. Sci.* **105**, 19606–19611 (2008).
31. Devarakonda, S. B., Han, J., Ahn, C. H. & Banerjee, R. K. Bioparticle separation in non-Newtonian fluid using pulsed flow in micro-channels. *Microfluid. Nanofluidics* **3**, 391–401 (2007).
32. Strohmeier, O. et al. Centrifugal microfluidic platforms: advanced unit operations and applications. *Chem. Soc. Rev.* **44**, 6187–6229 (2015).
33. Waheed, S. et al. 3D printed microfluidic devices: enablers and barriers. *Lab Chip* **16**, 1993–2013 (2016).
34. Siller, I. G. et al. 3D-printed flow cells for aptamer-based impedimetric detection of E. coli crooks strain. *Sensors* **20**, 4421 (2020).
35. Contreras-Naranjo, J. E., Perez-Gonzalez, V. H., Mata-Gómez, M. A. & Aguilar, O. Cost-effective 3D-printed-enabled fluidic electrochemical sensing platform for quantitative electroanalytical applications. *J. Electrochem. Soc.* **168**, 117504 (2021).
36. Chen, S. et al. Microfluidic device directly fabricated on screen-printed electrodes for ultrasensitive electrochemical sensing of PSA. *Nanoscale Res. Lett.* **14**, 71 (2019).
37. Kuscer, D. et al. An advanced miniature fluidic system in multilayer ceramic technology with precise temperature and flow control for in situ pollution monitoring. *Sens. Actuators A Phys.* **366**, 114946 (2024).
38. Ruiz-Vega, G., Garcia-Berrocoso, T., Montaner, J. & Baldrich, E. Paper microfluidics on screen-printed electrodes for simple electrochemical magneto-immunosensor performance. *Sens. Actuators B Chem.* **298**, 126897 (2019).
39. Assudani, P. J. et al. Artificial intelligence and machine learning in infectious disease diagnostics: a comprehensive review of applications, challenges, and future directions. *Microchem. J.* **218**, 115802 (2025).
40. Mao, R. et al. Integrated biosensing platform based on Bi 2 S 3 /BiFeO 3 heterojunction and BiVO 4 for ultrasensitive organic photoelectrochemical transistor and colorimetric dual-mode detection of prostate-specific antigen. *Anal. Chem.* **98**, 787–798 (2026).
41. Sekhwama, M., Mpofu, K., Sudesh, S. & Mthunzi-Kufa, P. Integration of microfluidic chips with biosensors. *Discov. Appl. Sci.* **6**, 458 (2024).
42. Lokar, N., Pečar, B., Možek, M. & Vrtačnik, D. Microfluidic Electrochemical Glucose Biosensor with In Situ Enzyme Immobilization. *Biosensors* **13**, 364 (2023).
43. Kurul, F., Avci, M. B., Bertan Acar, H., Topkaya, S. N. & Cetin, A. E. Incubator-integrated electrochemical analysis platform for cell-based studies. *npj Biosensing* **2**, 6 (2025).
44. Su, W.-Y., Wang, S.-M. & Cheng, S.-H. Electrochemically pretreated screen-printed carbon electrodes for the simultaneous determination of aminophenol isomers. *J. Electroanal. Chem.* **651**, 166–172 (2011).
45. Rantataro, S., Ferrer Pascual, L. & Laurila, T. Ascorbic acid does not necessarily interfere with the electrochemical detection of dopamine. *Sci. Rep.* **12**, 20225 (2022).
46. Kadara, R. O., Jenkinson, N. & Banks, C. E. Screen printed recessed microelectrode arrays. *Sens. Actuators B Chem.* **142**, 342–346 (2009).
47. Gornall, D. D., Collyer, S. D. & Higson, S. P. J. Investigations into the use of screen-printed carbon electrodes as templates for electrochemical sensors and sonochemically fabricated microelectrode arrays. *Sens. Actuators B Chem.* **141**, 581–591 (2009).
48. Oliveira-Brett, A. M., Piedade, J. A. P., Silva, L. A. & Diculescu, V. C. Voltammetric determination of all DNA nucleotides. *Anal. Biochem.* **332**, 321–329 (2004).
49. Xu, J. et al. A smartphone-mediated "All-In-One" biosensing chip for visual and value-assisted detection. *Anal. Chem.* **96**, 15780–15788 (2024).
50. Lee, K. et al. All-in-one platform for salivary cotinine detection integrated with a microfluidic channel and an electrochemical biosensor. *Lab Chip* **20**, 320–331 (2020).
51. Li, Y. et al. Organic electrochemical transceiver: An all-in-one sense-and-release device architecture for physiological modulation. *Sci. Adv.* **11**, 1–12 (2025).

Acknowledgements

S.N.T. acknowledges The Scientific and Technological Research Council of Türkiye (TÜBİTAK) (Project No. 123Z570).

Author contributions

S.N.T. served as the principal investigator, providing overall supervision and securing funding for the project. S.N.T. and A.E.C. conceptualized the study and designed the experimental framework. F.Ku., D.A., F.Ko., and A.E.C. developed the system hardware. F.Ku. and S.N.T. performed electrochemical experiments. D.T. and F.Ko. developed the system software and graphical user interface. F.Ku., A.E.C., and S.N.T. carried out signal processing and data interpretation. U.A. and A.K. performed the design, execution, and analysis of the CFD simulations. All authors contributed to the writing and editing of the manuscript and approved the final version.

Competing interests

The authors declare no competing interests.

Additional information

Supplementary information The online version contains supplementary material available at https://doi.org/10.1038/s44328-026-00083-0.

Correspondence and requests for materials should be addressed to Arif E. Cetin or Seda Nur Topkaya.

Reprints and permissions information is available at http://www.nature.com/reprints

Publisher's note Springer Nature remains neutral with regard to jurisdictional claims in published maps and institutional affiliations.

Open Access This article is licensed under a Creative Commons Attribution-NonCommercial-NoDerivatives 4.0 International License, which permits any non-commercial use, sharing, distribution and reproduction in any medium or format, as long as you give appropriate credit to the original author(s) and the source, provide a link to the Creative Commons licence, and indicate if you modified the licensed material. You do not have permission under this licence to share adapted material derived from this article or parts of it. The images or other third party material in this article are included in the article's Creative Commons licence, unless indicated otherwise in a credit line to the material. If material is not included in the article's Creative Commons licence and your intended use is not permitted by statutory regulation or exceeds the permitted use, you will need to obtain permission directly from the copyright holder. To view a copy of this licence, visit http://creativecommons.org/licenses/by-nc-nd/4.0/.

© The Author(s) 2026